6

Visible light, wide-angle graded metasurface for back reflection

There's a rhythm and rush these days
Where the lights don't move and the colors don't fade

Stay alive – José González

Metasurfaces, or phase-engineered quasi-2D interfaces, enable a large degree of control over the reflection, refraction and transmission of light. Here we demonstrate the design and realization of a visible light gradient metasurface tailored for highly efficient back reflection based on the Huygens–Fresnel principle. The metasurface emulates the functionality of a Littrow grating, capable of efficiently channeling light into the first negative Floquet order over a broad angular range and bandwidth at visible frequencies. Our theoretical results predict unitary efficiency for extremely low profiles and an optical response that is robust against discretization and design modifications. The experimentally realized metasurface is comprised of high-index TiO_x nanowires over a protected Ag mirror, enabling back reflection with efficiency above 85% in the visible range, close to the reflectivity of the bare silver mirror. The presented analytical design methodology and the resulting low-profile device are advantageous compared to conventional gratings, while offering broadband efficiencies over a range of incidence angles.

6.1. Introduction

Gradient metasurfaces have started to significantly influence modern optical technology as they offer the possibility of replacing a wide range of bulky optical components with low-profile and low-loss patterned surfaces [97–100]. Graded metasurfaces rely on nanostructured surfaces with controlled variation of their transverse impedance, enabling a plethora of operational possibilities, including anomalous wave refraction and reflection [101, 102], holography [103, 104], cloaking [105–107], focusing and beam shaping [101, 108], polarization management [65, 109], and nonreciprocal beam control when combined with time modulation [110, 111]. The nanoscale control of strong wave-matter interactions in metasurfaces has opened remarkable opportunities for low-loss, integrable planar optics [98]. In contrast to other ultrathin configurations based on resonantly excited elements [112–116], gradient metasurfaces typically rely on the response of a combination of non-resonant scatterers and their tailored arrangement, enabling this class of metasurface to support inherently broadband and robust optical responses which are resilient to losses [109]. In this work, we apply the concept of graded metasurfaces to design broadband back reflectors, based on distributed surface impedances. Back reflectors are a class of periodic structures that are specifically tailored to funnel the incident energy into the first negative order Floquet harmonic. These structures are traditionally implemented using binary patterns over finite thicknesses [114, 117–119], which typically need to be optimized to maximize the coupling efficiency to the backward Floquet order [119, 120]. Here we use an alternative method based on the Huygens–Fresnel principle to define the ideal surface impedance profile of ultrathin metasurfaces that enables arbitrary negative reflection. The ideal operation of the designed surface is achieved by controlling the required secondary scattering sources on the metasurface to reconstruct the desired Floquet order. This approach offers flexibility in design, avoiding the need for optimization or specific material parameters, and enables high back-reflection efficiencies over the desired range of angles of incidence (AOI), angles of reflection and frequency. In order to validate our theoretical approach, we employ high-resolution nanolithography to experimentally implement a back reflecting graded metasurface that operates in the visible range.

6.2. Results and discussion

First, we focus our study on the design of an ideal gradient metasurface that reflects all the impinging energy back to the source for a specific frequency and angle for linear polarized light; essentially operating as a zero-thickness Littrow grating. This functionality is equivalent to an ideal retroreflector for this frequency and AOI (Fig. 6.1A shows the concept and a schematic of the fabricated structure). While an ideal homogeneous mirror (Fig. 6.1B) reflects the impinging light towards the specular direction due to momentum conservation, this ideal metasurface with a tailored gradient of the reflection phase (Fig. 6.1C) can impart a suitable additional negative transverse momentum to the impinging wave and reflect the entire impinging light flux back to the source.

Following the approach introduced in [101, 108], and tailored to efficiently manipulate reflected beams in [109], we derive in the Methods section (6.4.1) the analytical expression of the local reflection coefficient that an ultrathin metasurface needs to sup-

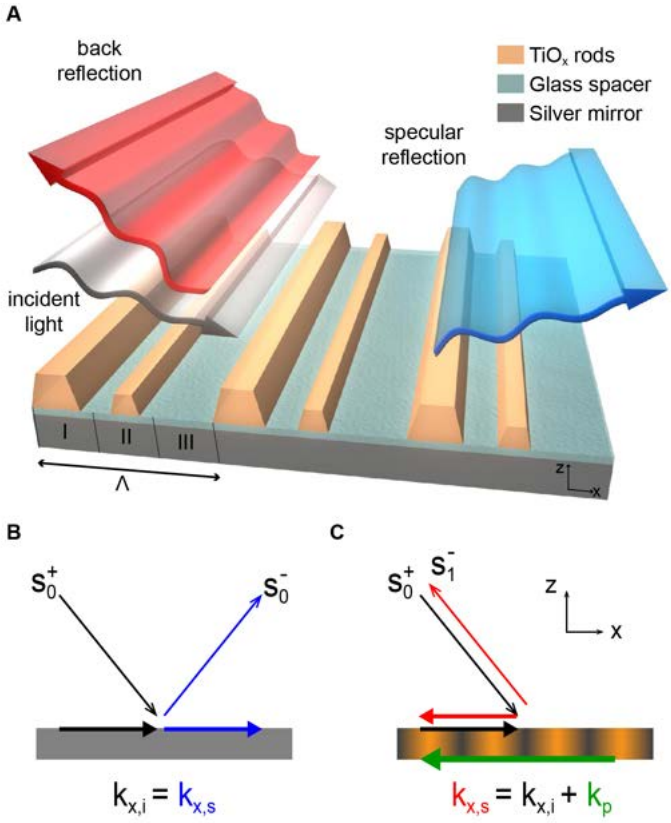

Figure 6.1: Operation principle of a metasurface back reflector. (A) Schematic illustration of back-reflection from a gradient metasurface. (B) Representation of specular reflection from an ideal mirror: incident light (s_0^+, black) is specularly reflected (s_0^-, blue) from an ideal mirror due to momentum conservation at the interface. (C) Scattering channels for reflection from a gradient metasurface: incident light is reflected back (s_1^-, red) toward the source due to the transverse momentum imparted by the inhomogeneous interface. The additional negative momentum k_p (green) is introduced by a tailored gradient of the reflection phase. Momenta in the x-direction are shown by $k_{x,i}$ and $k_{x,s}$ for incident and reflected waves, respectively.

port in order to achieve single-angle retroreflection with unity efficiency for illumination angle θ_0 in the $x-z$ plane, where $\hat{z}$ is the direction normal to the surface:

$$r(x) = \frac{-1+\cos\theta_0 - e^{\frac{2i\pi x}{\Lambda}}(1+\cos\theta_0)}{-1-\cos\theta_0 + e^{\frac{2i\pi x}{\Lambda}}(-1+\cos\theta_0)} \tag{6.1}$$

The required reflection coefficient is unitary all across the surface, implying that it can be achieved with a fully passive interface with inhomogeneous phase profile $\varphi(x)$, shown in Fig. 6.2A for $\theta_0 = 35.7$ degrees, with period $\Lambda = \frac{\lambda}{2\sin\theta_0}$, where λ is the wavelength of operation in free-space. In general, the optimal reflection coefficient of a gradient metasurface may also involve local amplitude modulation [121]. At the retroreflection angle, however, the exact impedance matching between the incident and scattered

beam guarantees that 100% wave conversion is accessible using a purely lossless surface profile, as described by the local phase variations in Eq. 6.1. This nonlinear phase profile exactly compensates for the momentum mismatch between the incoming and the desired retroreflected waves (Fig. 6.1C). For values of incident wave different from θ_0, the reflected wave does not align with the incident wave and the structure operates as an ultrathin back reflector, redirecting light back into the half-space of incidence. Compared to previous attempts to realize highly efficient back reflecting gratings, this approach is fully analytical, where calculations based on the Huygens–Fresnel principle allow us to engineer the scattering pattern over an infinitesimally thin surface at will, and without requiring iterative optimization [68, 121]. For instance, the surface may be equivalently designed to couple a desired portion of the impinging power toward the specular reflection, and the other portion toward back reflection. This concept is also fully extendable to two-dimensional surfaces and arbitrary polarization control.

For an ideal continuously modulated metasurface with a local reflection given by Eq. 6.1, given the periodicity of the modulation the reflected power can couple to only two propagating diffraction orders, the specular reflection s_0^- and the first negative Floquet order s_1^-. The numerically calculated coupling efficiency to these orders as a function of illumination angle is shown in Fig. 6.2B for the surface with phase profile in Fig. 6.2A (see Supplementary Note 1 (6.5.1)). As expected, we obtain 100% coupling efficiency at $\theta_0 = 35.7$ degrees (the design angle), i.e., $s_1^- = 1$. For this AOI, the metasurface operates in the Littrow configuration and the angle of reflection equals 35.7 degrees. In addition, the figure shows that the angular response is robust. For an AOI range $11 < \theta_{in} < 80$ degrees over half of the incident power is redirected into the non-specular direction, despite these angles residing outside of the Littrow design parameters. This broad angular response is associated with the fact that the momentum imparted by the surface does not change with the incidence angle [101], and it is sufficiently negative to ensure that the angle of the emerging reflected beam stays negative over a broad angular range. In general, the attainable angular range may be further increased by designing the retroreflection angle close to 45 degrees. The back reflection angle varies as a function of impinging angle following the grating equation for first-order diffraction $\theta_{back} = \arcsin(\sin\theta_{in} \pm \frac{\lambda}{\Lambda})$, where the $\pm$ sign refers to $\theta_{in} > 0$ and $\theta_{in} < 0$ respectively, as plotted in Fig. 6.2C. The lower cut-off for $\theta_{in} = 11$ degrees is simply determined by the cut-off of s_1^- for close-to-normal incidence, and it can be adjusted by design.

An interesting feature evident in Fig. 6.2B is the perfectly symmetric response of the back reflective surface. The symmetry arises despite the fact that the geometric profile of the surface, described by Eq. 6.1, is asymmetric and tailored for a specific oblique illumination. This symmetry is a general result stemming directly from reciprocity [122, 123], and it is not limited to our particular configuration. More specifically, if the surface is designed to back reflect with x% efficiency for the AOI θ_{in}, it ensures (100-x)% coupling to the specular direction ($\theta_r = \theta_{in}$). Reciprocity then ensures that, when the direction of illumination is flipped and the surface is illuminated from the specular direction, exactly (100-x)% of the power can be coupled back towards θ_{in}. The remaining x% of the power must be scattered through the only remaining scattering channel which is the corresponding back reflection. Given that the period is unaffected by the incidence direction, and it is designed to admit only two diffraction orders, all remaining energy (x%)

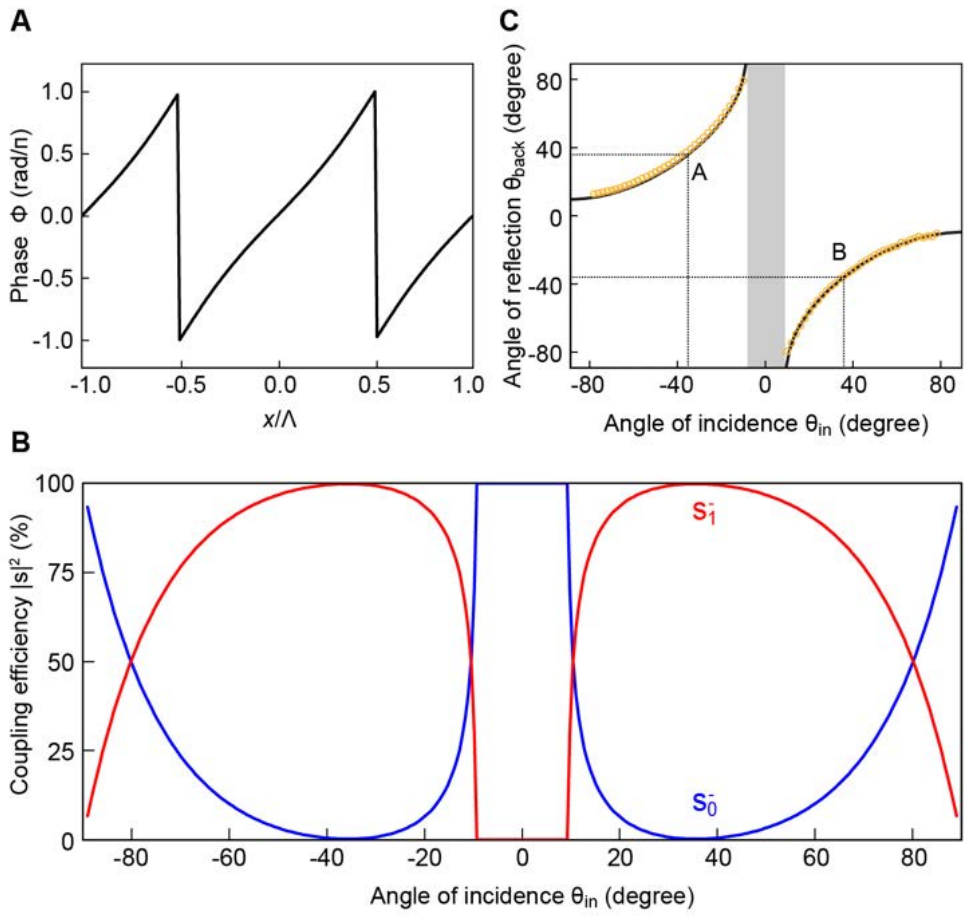

Figure 6.2: Wide angle operation of an ideal back-reflector metasurface. (A) Calculated local phase profile of the ideal surface $\Phi(x) = \angle(x)$, designed for retroreflection at AOI $\theta_0 = 35.7$ degrees following Eq. 6.1, with a surface period $\Lambda = \lambda/(2\sin(\theta_0))$. (B) Numerically calculated coupling efficiency of the ideal surface in panel (A) for different incident angles and for s-polarized illumination. Blue and red curves show the percentage of power coupled toward the specular direction (s_0^-) and first diffraction order (s_1^-), respectively. (C) Calculated (solid black line), and measured (yellow circles) angular dispersion of the gradient surface for the ± diffraction orders. The black lines correspond to the ideal surface in panel (A) and the yellow circles are analogous results measured at λ = 700nm for the fabricated sample. A and B correspond to the ideal retroreflection points where $\theta_{back} = -\theta_{in} = \pm 35.7$ degrees (Littrow configuration). Inside the highlighted gray region, the non-specular diffraction orders are evanescent.

will be coupled to the back reflected beam. Thus, the blue curve in Fig. 6.2C is center-symmetric and with the broad angular response in the negative half plane, reciprocity ensures an equally broad response for positive incidence angles.

The properties described so far are desirable from a practical standpoint, indicating that there is no trade-off between directionality and efficiency in the proposed metasurface, and back reflection can be achieved over a broad range of angles, even far from

normal incidence. This property also suggests an interesting possibility for applications in the retroreflection industry. While the designed surface is not a true retroreflector, for detectors using narrowband illumination and a relatively wide collection aperture this surface may reflect nearly all of the impinging energy back to the source. Another interesting application of this surface might be replacing the diffusive retroreflective tapes (over a limited angle), as the efficiency of reflection is significantly larger than available reflective tapes and the metasurface can be tailored to operate for extremely broad AOI range [124].

In order to practically realize the proposed metasurface we need to discretize the ideal phase profile (Eq. 6.1). Assuming an equal discretization of the ideal phase profile into N phase steps, the coupling efficiency to the retroreflected order gets closer to 100% as the number of steps increases (Supplementary Note 2 (6.5.2)). Interestingly, even a coarse discretization with only two discretization steps yields a retroreflection efficiency larger than 75%. The reason behind this robustness is again associated with the nature of our design. First, the diffraction phenomenon is non-resonant and therefore inherently robust to perturbations. Second, the period Λ determines two propagating diffraction orders for the operational frequency ensuring that, as long as the overall phase gradient along each unit cell suppresses the coupling towards the zero-th order diffraction (specular reflection), reflection will be funneled towards the first order in the back direction.

The ultrathin profile of the designed surface provides an ideal platform for microwave or terahertz graphene-based metasurfaces which are inherently deeply subwavelength. Here, we chose to realize the device characterized in Fig. 6.2A using a nanostructured dielectric metasurface operating in the visible spectrum (Fig. 6.3A-B) with subwavelength thickness t = 100nm, made of TiO_x trapezoidal bars on top of an Ag mirror via e-beam lithography and evaporation (see Methods for a description of the fabrication process (6.4.3) and Fig. 6.1A for a schematic of the fabricated structure). The dielectric nature of TiO_x and its relative high index (n=2.35 for λ = 500 nm to n=2.23 at λ = 1000 nm), are suitable to minimize absorption and provide reasonable phase control over a relatively small thickness [125]. We designed the structure with three phase discretization steps, N = 3, for operation at λ = 700 nm , tailored for s-polarized excitation (Electric fields lies in the metasurface plane). The variation of the local reflection coefficient in the first two elements is achieved by controlling the geometry of the nanorods. The third segment consists of the bare back-mirror (Fig. 6.3A).

The fabricated structure was excited with a weakly converging beam such that the excitation angle was well-defined. The reflected intensity was measured using an optical power meter (see Methods section (6.4.4) for more details on the measurement). The sample was mounted in the center and the power meter on the outer ring of a rotating stage, while the illumination direction was held constant. This enabled independent control of excitation and sampling angles, as depicted in the schematic of the measurement setup in Fig. 6.3C. We chose Λ = 600 nm (605 nm in the fabricated surface) to enable efficient back reflection in the free-space wavelength range λ = 490 - 940 nm.

The previous analysis ensures that an efficient back reflector can be implemented over a deeply subwavelength thickness. At shorter wavelengths, and specifically over the visible spectrum, current nanofabrication techniques limit the accessible resolution and accuracy of sub-hundred-nanometer features. To reduce the sensitivity of the device to

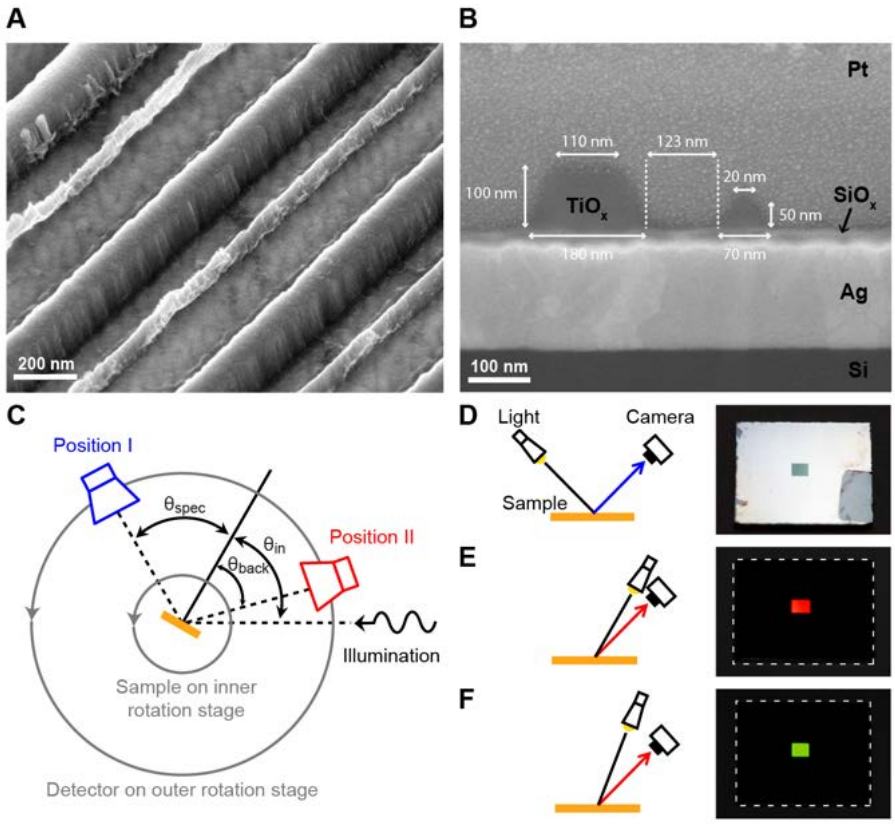

Figure 6.3: Fabricated structure and measurement setup. (A) SEM image (top view, under 40% tilt) and (B) cross section of the fabricated sample with extracted dimensions of the device. One unit cell of the structure is composed of three regions: two TiO_x nanorods and the bare mirror. See Methods section (6.4.3) for detailed geometry information. The Pt layer on top of the sample was added in the cross-section fabrication process to get a clean cross-section. (C) Schematic of the measurement setup: θ_{in} can be changed by rotating the sample on the inner rotation stage while the illumination arm is kept fixed. The coupling intensity to the different diffraction orders is measured by independently rotating the detector on the outer rotation stage to positions I to measure θ_{spec} or position II to measure θ_{back}. Illumination and detection planes are slightly tilted horizontally to allow retroreflection measurements without blocking the illumination. (D – F) Photographs of the fabricated structure on the right (1.5x1.5 mm^2 square in the center of the 12x12 mm^2 silver mirror, bare Si residual from fabrication process in the lower-left corner) and schematic of photography setup on the left. Panel (D) shows the specular response under illumination from the back with a commercial flashlight: no light is reflected in the specular direction from the structure (dark square in the middle). Panels (E – F) show efficient back reflection of the sample when illuminated with a white light lamp for different angles. The angle between light and camera was increased in (F) compared to (E).

nanofabrication errors we chose a thickness of t = 100 nm for the surface. The efficient operation of our fabricated sample from the practical observer standpoint is visualized in Fig. 6.3D–F. Photographs of the sample can be seen next to schematics of the photography setup. In Fig. 6.3D the bright specular reflection of the Ag mirror around the structure is visible while the dark square in the middle of the sample where the metasurface is placed indicates that specular reflection is almost absent. In contrast, the center of the sample is noticeably bright for an observer sitting close to the excitation source, as can be seen in Fig. 6.3E-F for different incoming angles. The bright color that can be observed in back-reflection depends on the angle of observation and illumination. As we mentioned previously, these pictures also indicate the possibility of utilizing these surfaces as efficient ultrathin retroreflectors for AOI close to the retroreflection angle. In this case, while the observable color of the reflected wave varies, the mirror covered with the designed metasurface is noticeably brighter than a conventional mirror.

The optical response of the fabricated sample is quantitatively demonstrated in Fig. 6.4. Symmetric scattering resulting from reciprocity permits a complete characterization of the device while scanning only half the angular range (Fig. 6.4A). However, to confirm the theoretical results we performed measurements over the full range of angles. In the figure, we compare the specular reflection to the measurements obtained using a flat silver mirror, similar to the ground plane utilized in our device, allowing a direct comparison that provides a quantitative calibration of the measured efficiency. The grey circles in Figure 6.4A present the measured angular response of the silver mirror when illuminated with s-polarized light at λ = 700 nm. We observe that around 10% of the incident power is lost, either through absorption or diffuse scattering. The measured response of the silver mirror is slightly lower than simulated reflectance using the tabulated dielectric response of single crystalline silver (Fig 6.4A). This difference is attributed to nanoscale surface roughness resulting from evaporation and other fabrication defects.

The level of back reflection of our sample is shown with red circles in Fig. 6.4A, demonstrating that most of the scattered light is indeed efficiently back reflected. The specular reflection thus significantly drops over a wide angular region around the retroreflective angle θ_0 = 35.7 degrees. The scattered power is focused toward the backward diffraction channel (s_1^- in Fig. 6.1C), yielding a coupling efficiency of 88% under illumination at θ_0 = 35.7 degrees, and with less than 10% of the impinging power being absorbed or diffusely scattered at the design frequency under illumination from all angles, except around the Wood's anomaly, consistent with the absorption levels obtained from the bare silver back-mirror. We note that the presence of the plasmonic mirror creates additional absorption at the metal-dielectric interface. For applications requiring the highest efficiencies, such as pulse shaping, stretching, and compression, the Ag mirror could be replaced with an optimized Bragg reflector.

Although the metasurface was originally designed for AOI of 35.7 degrees, increasing the incidence angle toward grazing angles does not significantly affect the overall efficiency and up to a remarkably large angle $|\theta_{in}|$ = 75 degrees, at λ = 700 nm the dominant portion of the scattered power remains in the same half-plane of the incident wave. For illumination at angles less than $|\theta_{in}| < 9$ degrees, the second scattering channel is non-radiative for λ = 700 nm , and thus it is not excited (Fig. 6.2C). Over this range, the metasurface operates as a simple mirror, as observed in Fig. 6.4A. For comparison, the

solid lines in Fig. 6.4A also show the calculated coupling to the two scattering orders obtained using full-wave simulation for a structure with the same geometry as the fabricated device (See Methods section for details about simulation (6.4.2)). The simulated results agree well with our experiment, even though a slightly lower cut-off at large angles is observed in the measured data compared to the calculated curves. This is due to the small size of our sample, as the area where the measurement beam hits the structure increases with higher incoming angles and exceeds the structure area for $|\theta_{in}| > 60$ degrees. In this angular range, part of the light is specularly reflected from the bare mirror adjacent to the metasurface.

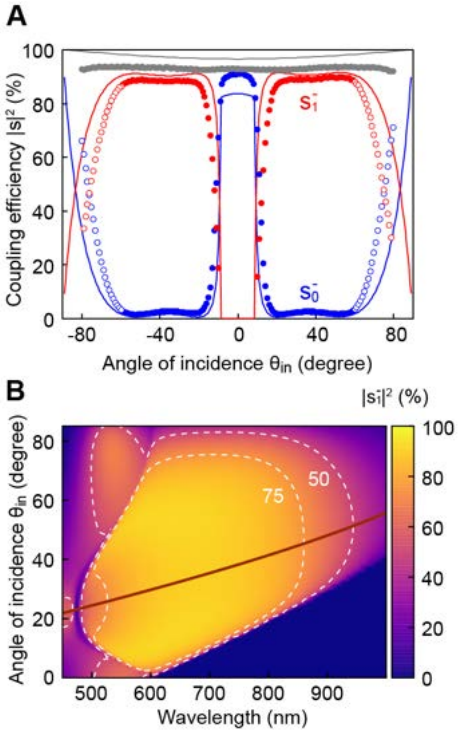

Figure 6.4: Back-reflection response of the fabricated device. (A) Angular response at λ = 700 nm. Comparison between measurements (circles) and numerical simulations (solid lines). Coupling efficiencies for the specular reflection s_0^- and the first-order negative reflection s_1^- , are shown with blue and red colors, respectively. The empty circles indicate reflection measurements for angles above $|\theta_{in}|$ = 60 degrees, for which the spot size of the beam exceeds the structured area and part of the beam is specularly reflected by the mirror next to the structure. The measurements and simulations of the bare mirror are depicted in grey. The homogenous surface supports specular reflection with approximately 10% absorption across all angles. (B) Numerical simulation results of the angular/frequency dispersion of the structure with the fabricated dimensions, showing the coupling efficiency toward the first-order negative reflection s_1^- and highlighting the 75%-power and 50% - power operation regions. The dark red line indicates the ideal retroreflective loci (Littrow configuration), for which the incoming and the reflected wave are aligned. More than 50% back reflection is achieved across λ = 490-940 nm and θ_{in} = 24-51 degrees.

A remarkable property of the back reflecting metasurface consists in its broadband

operation, which is attributed to the inherent stability of retroreflection as well as non-resonant nature of the involved scattering phenomenon, based on the phase gradient imposed through the metasurface. While the surface impedance of the trapezoids is expected to change over frequency, its relative slope across each unit cell is not significantly affected by frequency variations, ensuring that the net momentum imparted to the impinging wave still funnels most of the energy back to the first negative diffraction order. To further investigate this property, we determined the amplitude dispersion of the coupling to the two scattering modes for a structure with the dimensions of the fabricated device through full-wave simulations for all incident angles. As expected, the designed metasurface operates over an extremely broad half-power wavelength range λ = 490-940 nm in terms of single-angle retroreflection efficiency. We verified our simulations with experimental measurements at multiple wavelengths, in addition to the λ = 700 nm case, as reported in the Supplementary Note 3 (6.5.3). It is worth mentioning that the angular range and bandwidth of the grating may be further increased through optimization, however, here we presented a configuration derived directly by our analytical model in Eq. 6.1, also including all fabrication tolerances (e.g. height of second rod is smaller than t = 100 nm). A further discussion of the effect of shape and size of surface elements is given in Supplementary Note 4 (6.5.4).

The response of the designed metasurface is also controllable with the polarization of the incident wave. The surface features utilized for this implementation are inherently anisotropic, as their scattering properties depend on the orientation of the field vectors, and the local reflection phase is approximately constant for p-polarized illumination. Consequently, the surface operates as a simple mirror for this polarization, as discussed and verified in Supplementary Note 5 (6.5.5). In other words, this metasurface selectively reflects in opposite half-planes the two impinging polarizations. We are currently investigating polarization independent designs of back-reflecting metasurfaces based on a similar principle, achieved by considering 2D arrangements of isotropic surface elements [65, 109].

6.3. Conclusion

We have discussed the design principle and advantages in terms of size, simplicity of design and fabrication, bandwidth, acceptance angular range, low-profile and efficiency of gradient metasurfaces for back reflecting surfaces (i.e. ultrathin Littrow gratings). Indeed, we have shown that there is no fundamental limitation on the efficiency or size of a Littrow grating. One of the challenges in experimentally realizing the optimal surface profile derived in Eq. 6.1 is to achieve (semi-) continuous phase variation along the surface, which becomes important for large-angle operation, for which the required impedance profile has faster spatial variations [121]. We have shown here that coarse sampling of the optimal profile provides reasonably good performance over wide angular and frequency ranges at visible frequencies. Possible ways to overcome this limitation and gain higher efficiency (for larger retroreflection angle or more complicated functionalities) is to use Pancharatnam-Berry phase [126], where the local variation of the surface phase is achieved through rotation of a subwavelength nanoantenna. Continuously varying surface elements can also provide a solution to eliminate the requirements on surface discretization [127].

We believe that this approach is an effective replacement of conventional bulky optical elements, particularly for subwavelength gratings used in pulse shaping and spectrum splitting applications. The design is based on the Huygens-Fresnel principle and is scalable over different frequency ranges and may be modified for achromatic retroreflection at multiple frequencies (or AOI) [128, 129]. Similar designs may be explored at radio-frequencies to improve passive and active RFID tags. The control of the angle of reflection may also enable applications for light management in solar cells. The thin metasurface profile opens the possibility of spin coating or evaporating a thin absorber material on top of the metasurface, and broadband enhanced light trapping and absorption [109].

6.4. Materials and methods

6.4.1. Derivation of reflection coefficient

Derivation of the reflection coefficient: Following Huygens–Fresnel principle to achieve the arbitrary scattering field distribution, the electromagnetic boundary conditions of the system in Fig. 6.1C for s-polarized illumination read

$$\begin{aligned} 2\hat{z}\times(\boldsymbol{H}_i+\boldsymbol{H}_s)|_\sigma &= Y_e(x)\hat{y}\cdot(\boldsymbol{E}_i+\boldsymbol{E}_s)|_\sigma \\ -2\hat{z}\times(\boldsymbol{E}_i+\boldsymbol{E}_s)|_\sigma &= Z_m(x)\hat{y}\cdot(\boldsymbol{H}_i+\boldsymbol{H}_s)|_\sigma \end{aligned} \tag{6.2}$$

for any position x on the inhomogeneous metasurface σ, where Y_e and Z_m are the effective surface electric admittance and surface magnetic impedance of the structure [108, 109]. Subscripts i and s indicate the incident and reflected waves, respectively. The local reflection coefficient of the metasurface $r(x) = A(x)e^{j\Phi(x)}$ can be related to the effective properties of the surface for normal illumination as [108, 130]:

$$r(x) = -\frac{2(\eta_0^2 Y_e(x)) - Z_m(x))}{(2+\eta_0 Y_e(x))(2\eta_0 + Z_m(x))} \tag{6.3}$$

Considering plane wave excitation at θ_0 in the $x-z$ plane and ideal operation i.e. unity retroreflection the incident and scattered waves read

$$\boldsymbol{E}_{i,s} = \hat{y}E_0\exp(i(\hat{x}\cdot\boldsymbol{k}_{i,z}x+\hat{z}\cdot\boldsymbol{k}_{i,s}z)); \eta_0\boldsymbol{H}_{i,s} = \boldsymbol{k_{i,s}}\times\boldsymbol{E}_{i,s} \tag{6.4}$$

where $\boldsymbol{k}_i = k_0(-\sin(\theta_0)\hat{x}+\cos(\theta_0)\hat{z})$, $\boldsymbol{k}_s = -\boldsymbol{k}_i$, and k_0 is the free-space wave number. Combining Eq. 6.2,6.3 and 6.4 the local reflection coefficient is found as in Eq. 6.1. Note that the local reflection coefficient is merely a nonlinear phase distribution imprinted on the reflected wave as $A(x) = 1$. The phase profile for an ideal single-angle retroreflector with θ_0= 35.7 degrees is shown in Fig. 6.2A. The local phase profile increasingly deviates from linear distribution for larger values of θ_0 [121].

6.4.2. Numerical simulations

Numerical simulations throughout the paper were carried out by the 2D finite-element software COMSOL Multiphysics in the frequency-domain radio-frequency module. Periodic ports and Floquet periodicity boundary conditions are used to model one unit-cell of each metasurface. Ports are placed far enough from the metasurface such that

all evanescent scattering modes are sufficiently weak. The ideal back reflector characterized in Fig. 6.2 is modelled as a sheet admittance derived in Supplementary Note 1 (6.5.1). The substrate and free space are meshed with maximum element sizes of 2 nm and 26 nm, respectively. Perfect electric conductors are used in the ideal set up.

To model the fabricated device, we used the SEM images in Fig. 6.3A and 6.3B and estimated the dimensions as described in the fabrication process below. All materials are modelled as dispersive and lossy and we used realistic values for the permittivities of silver and SiO_x from experimentally retrieved datasets [131, 132]. For TiO_x, we measured the refractive index for a sample of on a Si wafer by spectroscopic ellipsometry. A maximum element size of 20 nm is used for high-index TiO_x rods and the remaining parts are meshed with a maximum element size of 28 nm. A 200 nm thick silver layer is used as the back reflector which we truncated with a perfectly matched layer to model a semi-infinite ground plane. The scattering parameters of the port are used to calculate the percentage of the power coupled toward each channel.

6.4.3. Fabrication process

A 1-mm-thick Si wafer was coated with 200 nm of Ag and 20-30 nm of SiO_x by thermal evaporation. This protected mirror was then spin-coated with ZEP520a, a high-resolution positive tone resist and Espacer 300z to improve the conductivity of the sample. Then the asymmetric grating was written by E-beam lithography using a 20 keV beam. The patterned area was 1.5 x 1.5 mm^2 square, comprised of stitched 100 x 100 μm^2 write fields. The sample was then rinsed for 30 seconds in water to remove the Espacer, developed in pentylacetate for 45 seconds, rinsed 15 seconds in a mixture of methyl isobutyl ketone and isopropanol (MIBK:IPA,9:1), dipped into IPA and transferred to ethanol. To prevent collapse of the fragile resist patterns the sample was dried at the critical point. The lines were filled with 100 nm of TiO_x by e-beam evaporation followed by lift-off which was done by dissolving the resist for 10 minutes in an ultrasonic bath in anisole. TiO_x was also evaporated directly on a Si wafer to allow a determination of the TiO_x dielectric function using spectroscopy ellipsometry, fitting the data using a Gaussian-Cauchy model. Completed dimensions were measured using a focused ion beam (FIB, FEI Helios Nanolab 600) to cut cross sections, with dimensions measured by electron micrographs. The metasurface consisted of repeating unit cells with a periodicity of 605 nm. The taller line had a height of 100 nm, a bottom width of 180 nm and a top width of 110 nm. The narrower line, separated from the tall line by a gap of 123 nm, had a height of 50 nm with bottom and top widths of 70 nm and 20 nm respectively (Detailed dimensions are shown in Fig. 6.3B).

6.4.4. Details of optical measurement

The coupling efficiency of the fabricated sample to the two orders was measured experimentally using a rotating stage, sweeping the angle of the incident plane wave across θ_{in}= -80 degree to θ_{in}= 80 degree. For illumination, a collimated broadband beam from a laser-driven light source (EQ-99X, Energetiq) was sent through a linear polarizer and then focused onto the sample with a weak lens. The focal point on the sample had a diameter of 0.75 mm. For excitation angles below 60 degrees the focus was smaller than the structure with an area of 1.5 x 1.5 mm^2; above this angle the light beam illuminated

both the structured region and part of the adjacent mirrored substrate. This resulted in measured intensities of specular and first order reflection with a slight contribution from the mirror. The intensity of the scattered power for the allowed scattering modes s_0^- and s_1^- was measured respectively for each degree using an optical power meter (Powermeter PM100USB with Photodiode Power Sensor S121C (Thorlabs)). The reflected beam was focused with a lens on the power sensor. To measure only the frequency ranges of interest an optical filter (either 700 nm, 750 nm or 850 nm center wavelength, 40 nm bandwidth, Andover Corporation) was placed in front of the lens of the power sensor.

6.5. Supplementary

6.5.1. Supplementary Note 1

We implemented the ideal phase profile in Fig. 6.2A following the method described in [109]. The variation in the phase of the local reflection coefficient is realized by varying the surface admittance at a subwavelength distance from a perfect electric conductor (ideal mirror). The obtained surface profile is modelled as a sheet admittance in COMSOL, with $h = \lambda/20 = 35$ nm for the distance between the sheet admittance Y_{surface} and the ground plane. In general, the relation between the local phase and the admittance reads:

$$\eta_0 Y_{\text{surface}} = -i \tan(\Phi(x)/2) + i \cot k_0 h \tag{6.5}$$

where $\Phi(x) = \angle(x)$ and η_0 is the characteristic impedance of free-space.

6.5.2. Supplementary Note 2

With the approximately linear phase profile in Fig. 6.2A, the metasurface performance is expected to be robust to surface discretization. Given that surface discretization is necessary in practical designs, here we investigate retroreflective efficiency (i.e. efficiency in Littrow configuration) for discretized realizations of the ideal surface shown in Fig. 6.2. For the ideal surface complete single-angle retroreflection is achieved for light incident at an angle of $\theta_{in} = 35.7$ degrees, and $\lambda = 700$ nm. The ideal local reflection phase is shown in Fig. 6.2A, and also shown in Fig. 6.5 (blue lines). Each period of the surface is then divided into N segments, and we increase N from 1 to 16. The case N=1 represents a fully homogenous surface and the case N=16 is a finely discretized surface for which the length of each step is 600/16 = 37.5 nm. For comparison, in Fig. 6.5 we also plotted the quantized reflection phase along the surface for the N=4 case. Following Supplemental Note 1 (6.5.1) we have numerically calculated the percentage of power coupled toward specular reflection and retroreflection for each discretization N (Fig. 6.6).

For N=1 the surface is a simple mirror that imprints a constant phase onto the specularly reflected wave s_0^-. Increasing the number of surface segments rapidly increases the power coupled into the first negative diffraction order s_1^-, with only two phase steps required to couple more than 75% of the incident power into this retroreflective order. We note that in this case the metasurface is still symmetric but the excitation asymmetry enforces an asymmetric scattering from the surface. For N=3, which corresponds to our physically implemented surface, a 90% efficiency in a lossless ultrathin structure is predicted. Quite interestingly, in experiments we obtained around 85% efficiency which is

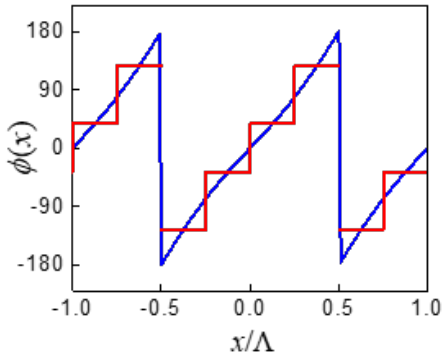

Figure 6.5: Discretized local reflection. Calculated ideal local phase profile of the surface $\Phi(x) = \angle(x)$, designed for an incoming angle of θ_0= 35.7 (blue line), and the discretized reflection profile for N=4 (red line). The surface period is Λ = 600 nm for operation at λ = 700 nm.

consistent with the amount of absorption from the back reflector (see Fig. 6.4A). Beyond this point ($N > 3$) the single-angle retroreflection efficiency is more than 98%, demonstrating the robustness of the metasurface response to surface discretization. For larger retroreflective angles, the optimal phase starts to deviate from linear shape and larger number of discretization are expected to be required.

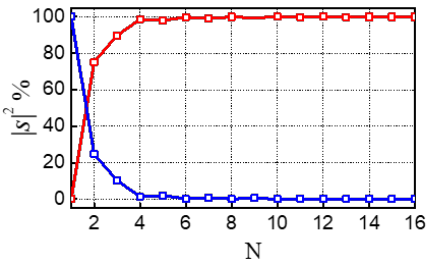

Figure 6.6: Effects of surface discretization. Coupling efficiency of the surface when the ideal continuous profile is discretized into N steps. Blue and red lines correspond to the numerically calculated coupling efficiency for an incident s-polarized wave at θ_{in}= 35.7 degrees, reflecting toward the specular direction (s_0^-) and retroreflection (s_1^-), respectively.

6.5.3. Supplementary Note 3

In addition to the measurements performed at λ = 700 nm on the fabricated sample (reported in Fig. 6.4A in the main text), we verified the broadband operation of the back reflector through analogous measurements at λ = 750 nm and λ = 850 nm. We sweep the angle of the incident plane wave from θ_{in} = -80 degrees to θ_{in} = 80 degrees. The intensity of the scattered power for the allowed scattering modes s_0^- and s_1^- is then measured experimentally as shown schematically in Fig. 6.3C. The results are compared in Figs. 6.7 and 6.8 with full-wave simulations of the metasurface, with dimensions obtained from

the fabricated device.

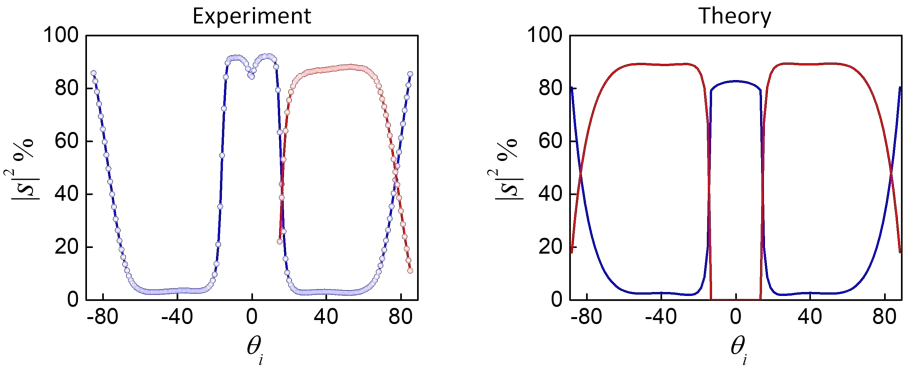

Figure 6.7: Angular response at 750 nm. Coupling efficiencies for the specular reflection s_0^- (blue) and the first-order negative reflection s_1^- (red) are shown: measurement (left) and numerical analysis (right) of the structure with the fabricated dimensions.

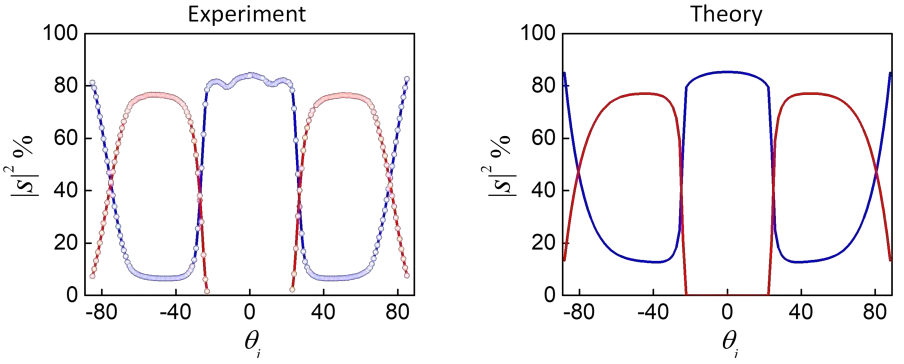

Figure 6.8: Angular response at 850 nm. Coupling efficiencies for the specular reflection s_0^- (blue) and the first-order negative reflection s_1^- (red) are shown: measurement (left) and numerical analysis (right) of the structure with the fabricated dimensions.

At $\lambda = 750$ nm we performed the measurement campaign only for half of the angular spectrum. As we discussed in the main text, reciprocity ensures that the distribution of the scattering amplitudes are symmetric with θ_{in}. The small irregularities observed in the measurement close to normal incidence are associated with polarization impurity of the incident light. Due to non-ideal alignment of the polarizer, the incident beam may contain a small fraction of p-polarized light. The response of the surface for p-polarized illumination is discussed in Supplementary Note 4 (6.5.4).

6.5.4. Supplementary Note 4

In this section and through series of numerical simulations, we study the effect of shape and size of nanorods on the response of metasurface. Fabrication errors may introduce

variations in the width and height of the nanorods and subsequently deteriorate the scattering response of the system. Intestinally, however, numerical simulations show that ±10% variations introduce only minor variations in the back-reflection response and coupling to the first negative order is almost constant (Fig. 6.9). This is consistent with our discussions on the non-resonant nature of the design. Furthermore, the exact shape of the nanorods is not a crucial parameter and the trapezoidal shape is simply chosen to facilitate fabrication process and avoid sharp corners. In this regard, the trapezoidal nanobars are replaced with rectangular bars (with equal mean widths) and the angular response of the system is shown in Fig. 6.10, also demonstrating very robust behavior with respect to the shape of surface elements.

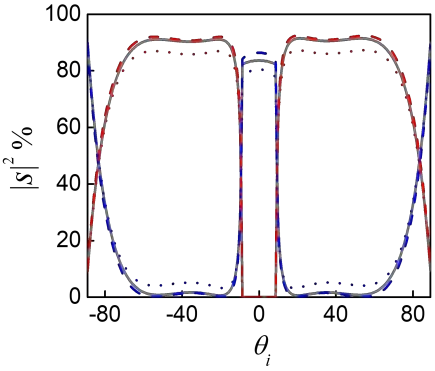

Figure 6.9: Tolerance to variations in the size of surface elements. Scattering response of the system considering +10% (dashed lines) and -10% (dotted lines) variations in heights and widths of surface elements while the period is kept constant. For comparison, grey lines also project the scattering response of the original surface. Specularly reflected power and the first order negative reflection are shown by blue and red colors, respectively.

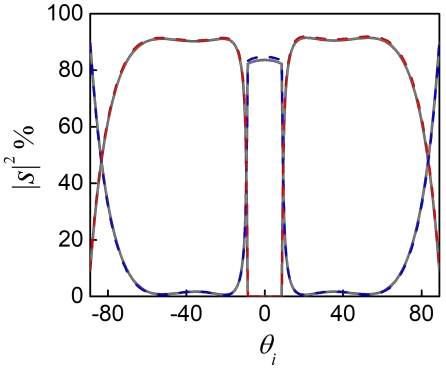

Figure 6.10: Tolerance to variations in the shape of surface elements. Scattering response of the system, replacing the original trapezoidal rods with rectangular rods (with equal mean widths). For comparison, gray lines project the scattering response of the original surface. Specularly reflected power and the first order negative reflection are shown by blue and red colors, respectively.

6.5.5. Supplementary Note 5

The metasurface is designed for s-polarized light, i.e.,light with electric field vector parallel to its plane. For s-polarized illumination, the majority of the incident wave is redirected toward the first diffraction order (which lies in the same half-plane as the incident one), creating a negative reflection effect. This effect is supported by the tailored distribution of local reflection coefficient for this polarization. On the other hand, under p-polarization the surface elements experience different local reflection phases due to their anisotropy. For measurements under p-polarized illumination, the surface is approximately a mirror, with around 15% coupling toward the non-specular diffraction channel and 15% absorption (Fig. 6.11, left panel). The measurements also show a critical incident angle for this polarization at which the incident light experiences enhanced absorption. Enhanced absorption at this angle is attributed to critical coupling between the free space mode and a grating resonance at the glass-silver interface. The measured reflection and absorption is confirmed via the corresponding simulations shown in Fig. 6.11 (right panel). We note that, by using isotropic surface elements in proper 2D arrangements, the metasurface can be designed to operate isotropically for both polarizations and 3D illumination angles [109]. We are currently exploring this possibility to create polarization insensitive back reflection.

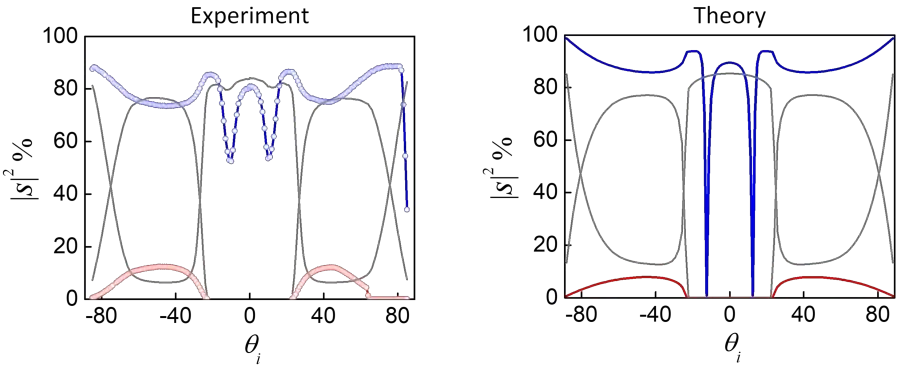

Figure 6.11: Scattering response for p-polarized illumination at 850 nm. Side-by-side comparison between measurement (left) and numerical analysis (right) of the fabricated device under p-polarized illumination. Specular reflection s_0^- the first-order negative reflection s_1^-, are shown with blue and red colors, respectively. To highlight surface anisotropy, the projected graylines show the corresponding response for s-polarized light, as in Fig. 6.8.